Reversible Optical Data Storage via Two-Photon Micropatterning of o-Carboranes embedded Switchable Materials

Stephania Abdallah, Rana Mhanna, Justo Cabrera-González, Rosario Núñez, Amine Khitous, Fabrice Morlet-Savary, Olivier Soppera, Davy-Louis Versace, Jean-Pierre Malval

Reversible Optical Data Storage via Two-Photon Micropatterning of *o*-Carboranes embedded Switchable Materials.

Stephania Abdallah[1], Rana Mhanna[1], Justo Cabrera-González[2], Rosario Núñez*[2], Amine Khitous[1] , Fabrice Morlet-Savary[1], Olivier Soppera[1], Davy-Louis Versace[3], Jean-Pierre Malval*[1].

[1]*Institut de Science des Matériaux de Mulhouse, UMR CNRS 7361, Université de Haute Alsace, 15 rue Jean Starcky, Mulhouse, 68057, France*
[2]*Institut de Ciència de Materials de Barcelona (ICMAB-CSIC), Campus U.A.B., 08193, Bellaterra, Barcelona, Spain.*
[3]*Institut de Chimie et des Matériaux Paris-Est, UMR-CNRS 7182, Equipe Systèmes Polymères Complexes, 94320 Thiais, France.*
Corresponding authors : Dr. Rosario Núñez (e-mail: rosario@icmab.es)
Prof. Jean-Pierre Malval (e-mail: jean-pierre.malval@uha.fr)

ABSTRACT.

Two-photon polymerization (2PP) constitutes a powerful light-triggered 3D stereolithography allowing the fabrication of micro- or nanostructures with spatially encoded functionalities. In the present report, we take benefit of this programmable property in order to develop of a photoresist authorizing the direct 2PP-lithography of luminescent switchable µ-structures. In this single step processing method, we highlight the pivotal role of a quadrupolar *o*-caborane initiator comprising a 9, 10-disubstituted anthracene core capable to chemically entrap oxygen inhibiting species during the free radical two-photon initiation step. Such an O_2 sequestration approach not only enhances the two-photon initiation performance of the polymerization but also generates a non luminescent endoperoxide by-product embedded in the polymerized macrostructure. Interestingly, a simple heating of the final materials promotes the endoperoxide thermolysis resulting in the recovery of the luminescent *o*-carborane dye. This original luminescence turn OFF/ON property exhibits an excellent fatigue resistance through a large number of alternated thermal and light stimuli cycles. The potential of this direct laser writing strategy for reversible data storage applications is finally demonstrated by two-photon patterning of a series of matricially organized µ-structures used as rewritable binary optical memories which can be easily encoded on demand.

KEYWORDS: Two-Photon lithography, *o*-carborane initiators, optical data storage.

1. INTRODUCTION.

Two-photon lithography (2PL) has emerged as one of the most promising additive manufacturing techniques which enables the micro- and nanofabrication of intricate architectures[1-3]. This maskless printing approach implies the raster scanning of a tightly focused *fs*-pulse laser within a photoresist which gives rise to the customized micro / nanostructures through a layer-by-layer slicing procedure. The high writing accuracy of 2PL stems from the intrinsic spatial confinement of the two-photon polymerization (2PP) reaction due to a primary two-photon absorption step which only occurs within an unsupported floating volume concentric to the excited focus. As a result, the elemental polymerized pixel can be generated with a drastically reduced dimension falling far below that of the optical diffraction limit. Therefore, 2PL not only displays a long range penetration depth into the photoresist (typically higher than 300 μm) but also constitutes a non diffraction limited technique which authorizes the fabrication of objects with arbitrary 3D geometries and complex nanoscale details. These two decisive advantages definitively make 2PL a truly 3D lithography able to spatially control the programmation of specific functionalities into the photopatterned materials[4]. With this respect, a very large panel of advanced functional materials has emerged from 2PL[1, 2, 4, 5]. For instance, the unprecedented properties of metamaterials in mechanic[6], acoustics[7], magnetics[8, 9] or optics[9-11] directly derived from the appropriate arrangement of a periodic pattern or lattice which is designed with a very fine adjustment of the size, shape and orientation. In this precise case, 2PL is perfectly adapted for modulating the metamaterials response since the related properties basically derived from a geometry tuning issue[10]. Another very popular strategy to spatially program the material consists in seeding a latent functionality either into the cross-linkable monomer or into the two-photon initiator both constituting the fundamental components of the photoresist. The latent property can then be activated after the 2PL fabrication. For instance, reconfigurable microstructures that can dynamically respond to distinctive local stimuli (pH, solvent, temperature) are fabricated following this construction guideline with the added value specifically centred on the cross-linking monomer. For instance, hydrogel / organogel photoresists clearly constitute one of the most popular materials toolboxes[11] whose stimuli-responsive properties have been extensively employed in plethora of micro objects such as drug delivery devices[12], soft microrobots[13], biomimetic self-actuators[14], stimuli-responsive shape-shifting μ-objects[15, 16]. The second alternative 2PL method consists in implementing the

added value into the two-photon initiating system. In this bottom-up approach, the two-photon initiator not only promotes the cross-linking reaction but disseminates concomitantly a novel functionality within the native macrostructure. For instance, the fabrication of conductive metallic structures without any extra deposition is inspired from this methodology where the two-photon initiator is also involved in a photoreduction reaction with a metallic salt incorporated in the photoresist[1, 17]. With this 'one pot' seeding approach, the resulted µ-object simply inherits its functionality from that of its related 2P-initiator leading to the fabrication of plasmonic resonators[18], SERS µ-sensors[19], catalytic µ-reactors[20], bactericidal photopatterned surfaces[21] or electrochemilumiscent devices[22]. In line with this direct laser writing method, we report herein a two-photon activable resist incorporating a multipolar *o*-carborane initiator with a dual functionality which combines 2PP initiation with a fluorescence ON/OFF switching through alternative thermal and light stimuli. Note that π-substituted carboranes are very robust compounds with high thermal and chemical stability that make them attractive for a wide field of applications[23] such as heat-resistant materials[24-28], thermo or mechanochromism[29], color-tunable devices[30-32] among others. In this report, we extend for the first time the applied potentials of *o*-carborane derivatives toward two-photon lithography. As depicted in **Scheme 1**, we present two distinctive dyes with a quadrupolar (**ACAR**) or octupolar (**XCAR**) architecture. Each system integrates an organic multibranched core playing the role of a π-electron relay constellated with bulky *o*-carboranes subunits at its external rims.

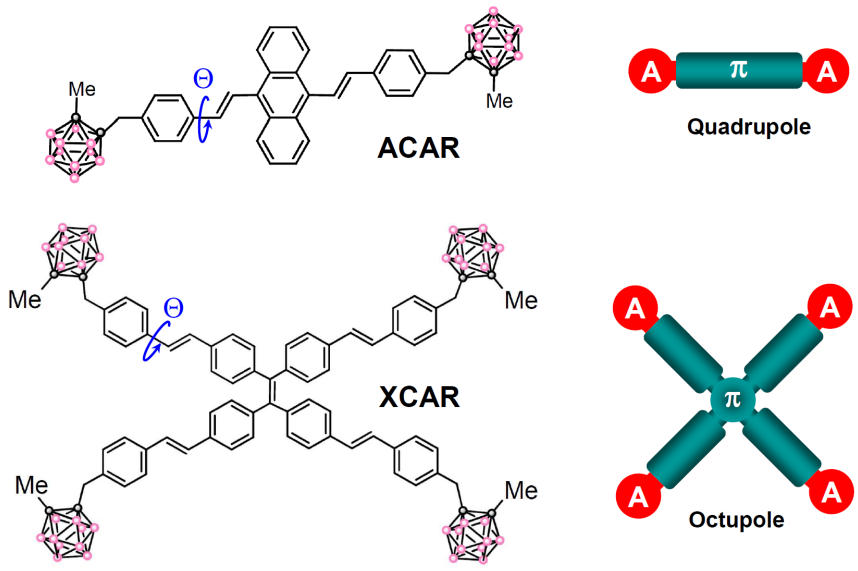

Scheme 1. Molecular structures of the *o*-carboranes along with their multipolar geometries.

These icosahedral boron clusters are well-known to be strong electron-withdrawing groups with a highly polarizable σ-aromatic character[23] which should efficiently promote a long-range π-electronic delocalization over their entire multipolar structure with subsequent benefit effects on the two-photon absorption cross-sections[33, 34]. We first provide a detailed investigation of the linear and non linear photophysical properties of these multibranched systems and compare their respective two-photon initiating reactivity. We then demonstrate how an additional side reaction inherent to the quadrupolar anthracene-based compound can be judiciously oriented to spatially encode at μm-scale a luminescence commutating functionality into the final materials.

2. RESULTS AND DISCUSSION.

The one- (1PA) and two-photon (2PA) absorption spectra of the molecules in dichloromethane (DCM) have been superimposed in **Figure 1** for a direct comparison of their respective absorption bands. **Table 1** gathers their corresponding spectroscopic data. In the low energy region, the 1PA spectrum of **ACAR** is dominated by a single absorption band with a moderate intensity (ε_{MAX} ~ 18 000 M^{-1} cm^{-1}) positioned in the 350-500 nm range. In the same spectral region, the 2PA spectrum clearly displays two well separated bands with a main intensity band at λ_{2PA}~ 710 nm exhibits a maximum 2PA cross-section (δ_{MAX}) of ca. 21 ± 3 GM. These two 2PA bands presumably echo two distinctive electronic transitions (i.e. $S_0 \rightarrow S_1$ and $S_0 \rightarrow S_2$ transitions[35]) located in the same energy region than those observed for the 1PA band. It should be noted that the lowest energy 2PA band has a very weak intensity with δ_{MAX} ~ 3 GM.

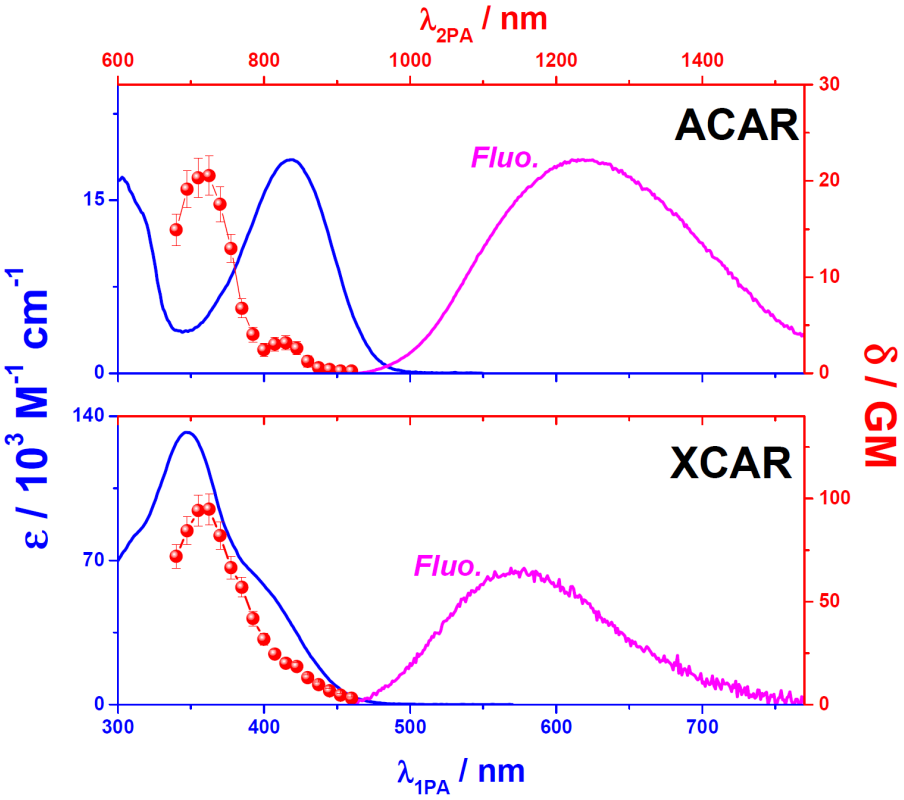

Figure 1. One- (full lines) and two-photon (circles) absorption spectra of the dyes in DCM. The fluorescence spectrum of each compound in DCM has been also added.

This low 2PA ability observed for the $S_0 \rightarrow S_1$ transition agrees with the 2PA dipole selection rule indicating that the lowest energy transition of a A-π-A quadrupole is theoretically two-photon forbidden. As shown in **Figure 1**, the 1PA band of **XCAR** is blue shifted as compared

to that of **ACAR** but presents much higher intensity of about 7-fold that of its quadrupolar homologue. This 1PA band is very broad and structured presumably due to the occurrence of multiple $S_0 \rightarrow S_n$ transitions[36]. Similarly to **ACAR**, the 2PA spectrum of **XCAR** does not match its 1PA one. This spectral effect is typically observed for centrosymmetric D_{2d} octupolar structures[37-40] for which the $S_0 \rightarrow S_1$ transition is also theoretically forbidden. As a consequence, the 2PA band positioned at 720 nm should be assigned to the $S_0 \rightarrow S_2$ transition. The corresponding δ_{MAX} is moderate with a value of about 95 ± 13 GM.

	ε_{abs} /10^3 M^{-1} cm^{-1}	λ_{abs} / nm	λ_{fluo} / nm	E_{00}[(a)] / eV	Φ_{fluo}	τ_{fluo} / ns	k_r [(b)] / 10^9 s^{-1}	k_{nr}[(b)] / 10^9 s^{-1}	$\frac{k_{nr}}{k_r}$
ACAR	18.5	417	605	2.70	0.12	1.23	0.10	0.72	7.2
XCAR	132.2	347, 395 [(s)]	577	2.75	0.02	0.64	0.03	1.53	51

[(a)] $E_{00} \approx \frac{1}{2} hc(\nu_{abs} + \nu_{fluo})$ in glassy matrix of 2MTHF. [(b)] $k_r = \Phi_{fluo} / \tau_{fluo}$, $k_{nr} = (1 - \Phi_{fluo}) / \tau_{fluo}$.

Table 1. Spectroscopic data of *o*-carborane compounds in DCM.

The fluorescence spectra of **ACAR** and **XCAR** in DCM are also presented in **Figure 1**. In both cases, the emission spectrum consists in a broad and structureless band located in the 500-750 nm range leading to a very large Stokes shift of about 7500 to 8000 cm^{-1}. This large spectral shift is a clear evidence of a strong electronic and/or geometrical change between ground and emitting states. In addition, the dyes are weakly emissive. This is especially true for the four-branched derivative with a fluorescence quantum yield (Φ_{fluo}) of 6-times lower than that observed for its two-branched homologue (see **Table 1**). This loss in emissivity is typically observed for π-conjugated multibranched chromophores[33, 34, 41]. It can be assigned to a large amplitude electronic relaxation at S_1 state, leading to an electronic symmetry breaking between the unrelaxed Franck-Condon state giving rise to an electronic delocalization that implies a full delocalization over the entire π-conjugated structure and the relaxed emitting state, whose excitation is localized more specifically on a single branch of the dye. Moreover, the molecular dimensionality of the system amplifies the efficiency of this non radiative deactivation process. This latter effect can be nicely exemplified here by comparing the nonradiative-to-radiative rate constants ratios (k_{nr} / k_r) which are multiplied by a factor ~ 7 on going from **ACAR** to **XCAR** (see **Table 1**). Interestingly, the excitation localization on a single branch of the dye can be also accompanied by a concomitant conformational change of the molecular structure. In order to demonstrate this interesting property, we measured the

fluorescence temperature dependence of the compounds in a glass forming solvent such as 2-methyltetrahydrofuran (2MTHF). **Figure 2** shows the fluorescence bands evolution of the dyes in 2MTHF by decreasing temperature. From 300 K to 80 K, the fluorescence quantum yields of **ACAR** and **XCAR** are respectively amplified by a factor 5 and 17 concomitantly with the decrease of their Stokes shift by a factor 4 and 2.5.

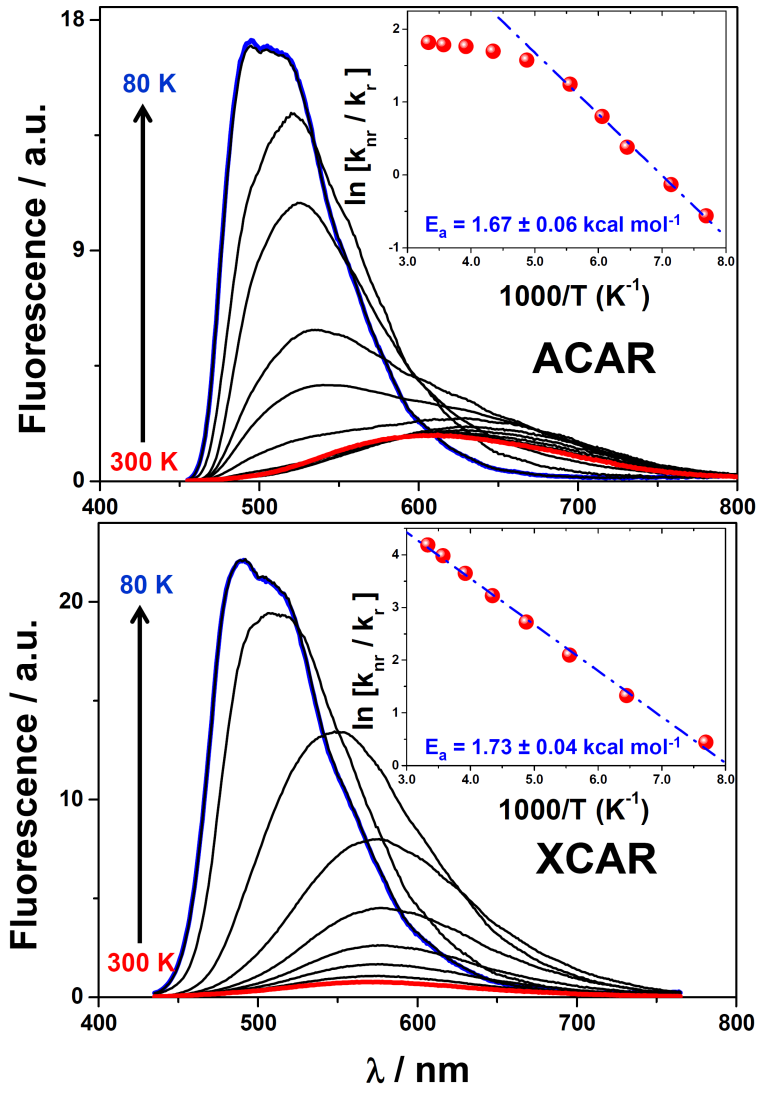

Figure 2. Fluorescence spectra of **ACAR** and **XCAR** in 2MTHF over temperature range 80-300 K. Insets: Arrhenius plot for the nonradiative-to-radiative rate constants ratio.

A detailed analysis of the fluorescence spectra shows two distinctive behaviours during the cooling process as depicted in **Figures S1 and S2**. From 300K to 230 K (the high temperature region), both fluorescence bands slightly shift to the red region with an increase in intensity. However, below this temperature range, the band red shifts are clearly levelled off. The further cooling of **XCAR** shifts its fluorescence band to the blue region whereas the same

cooling sequence results in the emergence of an unexpected blue emission band in the 470-570 nm range for **ACAR**. Note that this new fluorescence band rapidly increases nearby the glass-transition temperature (T_g ≈130 K) with a subsequent disappearance of the red fluorescence one. It should be also indicated that this dual emission does not result from emissive conformers at the ground state since the excitation spectra recorded from both emission bands perfectly match each others suggesting that the two emitting species derive from the same S_1 state. It is well known that excited states relaxation is both influenced by the solvent dielectric constant as well as the solvent viscosity[42]. However for 2MTHF, the relative impact of these two parameters can be sequentially discriminated depending on the temperature range. In the high temperature region, the fluorescence bathochromic effects observed for both compounds should be attributed to the enhancement of the medium polarity since the dielectric constant of 2MTHF continuously increases from 7 to 18 upon cooling[43-45]. In low temperature region nearby the glass-transition of 2MTHF, this dielectric constant drastically drops to 2.6 and remains constant whereas the viscosity enhances by 17 orders of magnitude up to 3.5 x 10^{19} Pa s^{-1}. As a consequence, the strong fluorescence enhancement observed in low temperature region should be mainly attributed to a viscosity-induced hindering effect which drastically hampers any conformational changes at S_1 state. With this respect, a *trans-to-cis* photoisomerization hypothesis can be first excluded since the absorption spectra of our stilbenyl chromophores remain perfectly invariant upon UV-irradiation in N_2-degassed solutions. Similarly to the twisting relaxation mechanism established by Lapouyade *et al.*[46-48] for donor-acceptor substituted stilbenes, we proposed that the photoinduced conformational change observed for **ACAR** and **XCAR** proceeds via an intramolecular twisting mechanism from a local excited state with a nearly planar stilbene conformation to a perpendicular one implying the rotation of the external *o*-carborane benzyl moiety around the central C-C bond as illustrated in **Scheme 1** (Θ ≈ 90°). This twisted geometry is expected to present a forbidden optical transition which accounts for the non- or weakly emissive character of this relaxed excited state. The proposed precursor-successor mechanism is in line with the dual emission of **ACAR** whose band intensities reversely evolve by decreasing temperature. The Arrhenius plots of ln (k_{nr} / k_r) *vs.* 1 / T are also presented in **Figure 2**. For both dyes, the correlations are sufficiently linear in the low temperature region to derive activation energies in the 1.6-1.8 kcal mol^{-1} range. These values nicely coincide with the viscosity barrier of 2MTHF (~ 1.82 kcal mol^{-1} [49]) and corroborates the barrierless character of these twisting conformation changes.

ACAR and **XCAR** have been employed as two-photon initiators for free radical polymerization. With this respect, they have been associated with an aliphatic amine reactant such as the N-methyl diethanolamine (**MDEA**). In this bi-component approach[50] (see **Figure 3**), a photoinduced electron transfer (PeT) can be promoted between the two-photon excited chromophore acting as an electron acceptor species and **MDEA**. Assuming that the photoinduced electron transfer proceeds from the S_1 state, the free energy (ΔG_{eT}) associated to the mechanism can be estimated according to the Rehm-Weller equation:

$$\Delta G_{eT} = E_{ox} - E_{red} - E_{00} + C \qquad (1)$$

In this formalism, E_{ox} corresponds to the oxidation of **MDEA** whereas E_{red} and E_{00} denote respectively the reduction potential and the S_1 state energy of the dye. Moreover the coulombic energy term C which characterizes the interaction of the generated radical ion pairs can be neglected in polar media. The oxidation potential of **MDEA** (E_{ox} = 0.93 V/SCE) and the reduction potentials of the *o*-carborane derivatives (E_{red} = -1.60 V/SCE for **ACAR** and -1.68 V/SCE for **XCAR**) have been evaluated by cyclic voltammetry in dichloromethane (see **Figure S3**). Therefore ΔG_{eT} can be estimated to values of - 0.17 eV for **ACAR** and - 0.14 eV for **XCAR**. These negative driving forces reasonably suggest that both PeT are thermodynamically allowed. Interestingly, the consecutive oxidation of **MDEA** generates an unstable amine-centred radical cation (**MDEA**$^{\bullet+}$) which rapidly deprotonates to form a neutral radical species[51] (**MDEA**$^{\bullet}$).

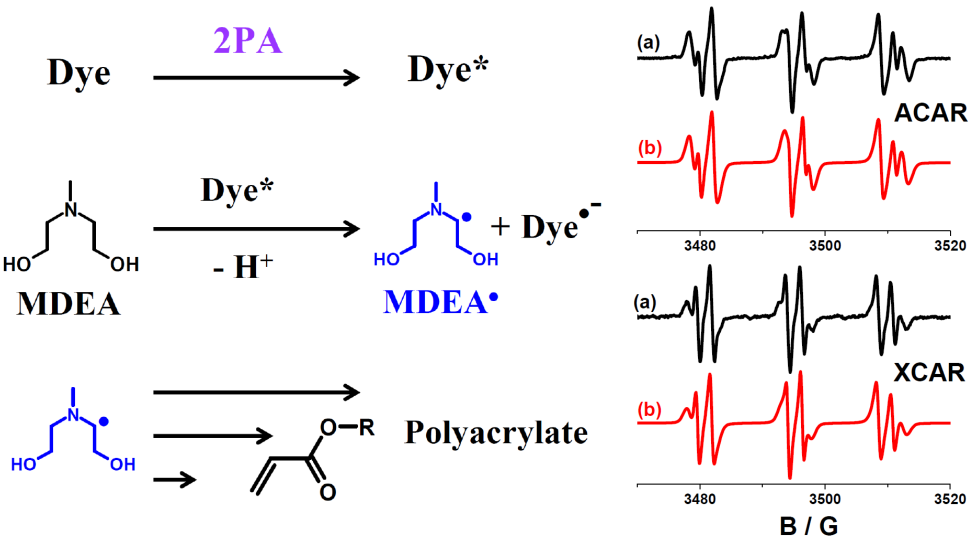

Figure 3. (Left side) Two-photon polymerization mechanism based on a bi-component free radical initiation strategy. (Right side) (a) ESR spectrum of spin trap adducts generated after irradiation of **ACAR** or **XCAR** mixed with **MDEA** in presence of **PBN**. ($\lambda_{irr.}$ = 365 nm. Solvent: *tert*-butyl benzene) (b) Simulated spectrum.

The generated α-aminoalkyl radical exhibits a very high reactivity upon addition reactions[52] on acrylates C=C bonds leading to a very efficient initiation process for free radical polymerization. The formation of **MDEA•** appears to be a crucial species for the 2PP efficiency and can be identified by ESR-spin trapping measurements. **Figure 3** typically shows the ESR-spectra of spin adducts which were produced during the irradiation of each bi-component system (dye + **MDEA**) in presence of α-phenyl-N-tertbutylnitrone (**PBN**) used as a spin trap reactant. Both ESR spectra are dominated by the signal of the α-aminoalkyl adduct of **PBN** showing an hyperfine coupling constants (a_N = 14.4 and a_H = 2.2 G) which agree very well with those previously reported[53].

To demonstrate the applied potential of our multibranched *o*-carborane derivatives for multiphoton 3D stereolithography applications, each bi-component system has been associated with an acrylate-based formulation comprising 67 mol% of a poly(ethyleneglycol)diacrylate monomer (**PEGDA**), where the carborane-based molecules were perfectly soluble at mM range and 33 mol% of pentaerythritol triacrylate cross-linker (**PETIA**). The addition of this latter trifunctional monomer should guarantee a better mechanical and geometrical integrity of the two-photon patterned structures. The formulations were prepared at isomolar concentration of dyes (1.5 mM) and with 3 %-w of **MDEA**. **Figure 4** shows several SEM images depicting various 3D µ-structures with arbitrary geometries fabricated at 800 nm: *i)* A polymer boat rudder with a 10 µm diameter fabricated using **ACAR** formulation. *ii)* A 15 µm diameter pumpkin-like object fabricated based on **XCAR** formulation using the same condition *iii)* A 35 µm-high screw with 1 µm pitch photopatterned with the same **XCAR** formulation. Interestingly, each µ-structure displays a surface roughness which illustrates the point-by-point fabrication procedure. Indeed, each 3D microstructure is obtained through a layer-by-layer assembly process obtained by *z*-stacking of several fused photopatterned planes. In the same manner, these polymerized planes are fabricated by two-photon curing along the scanning paths of the laser beam. The minimum polymerised volume element (‘voxel: volume pixel’) generated after the beam translation should fused with its adjacent voxel to ensure the mechanical integrity of the slice. It is precisely such voxel overlapped effects that create roughness at the external surface of the 3D microstructure.

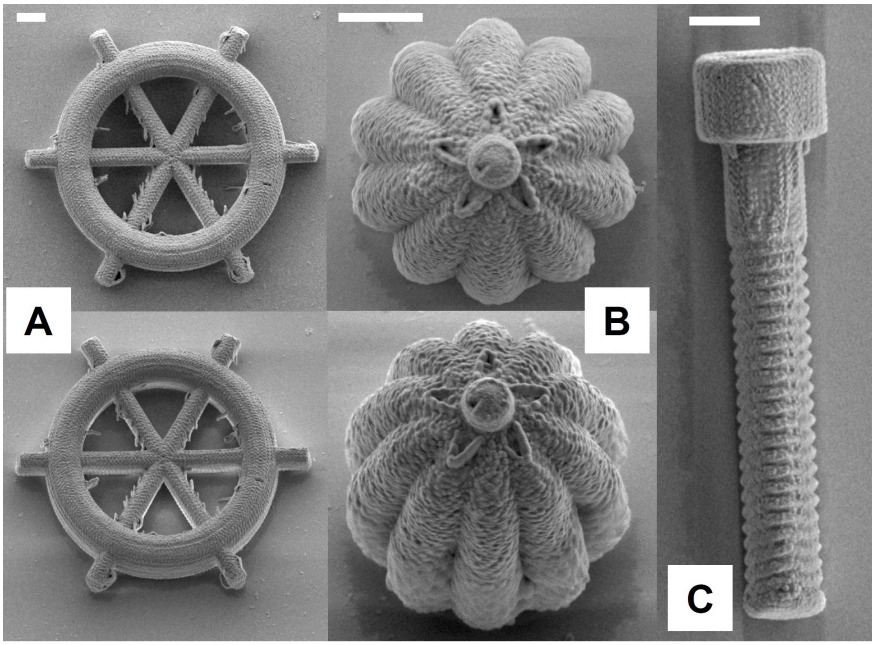

Figure 4. SEM micrographs of various two-photon polymerized µ-structures fabricated at 800 nm using **ACAR** (**A**) and **XCAR** (**B**-**C**) formulations (scale bars = 5 µm).

The writing speed performances of our *o*-carborane-based photoresists have been compared to each other. For this purpose, a series of square frames with 20 µm side were two-photon patterned by gradually increasing the direct laser writing speed in order to estimate the maximum value of the fabrication speed which guarantees a good quality of the model structure. For each formulation, **Figure S4** shows a typical transmitted micrograph of each µ-structure with its corresponding writing speed. According to such a qualitative screening test previously proposed by Liska *et al.*[54-57], it can be inferred that the photoresist with **XCAR** authorizes a maximum writing speed of about 400 µm s^{-1} which is ~1.8-fold higher than that measured for **ACAR** formulation in the same conditions. In order to compare more precisely the 2PP performances of **ACAR** and **XCAR**, we have also evaluated the polymerization energy threshold (E_{th}) of their respective isomolar photoresists. This photonic parameter corresponds to the minimum local absorbed-energy density necessary to observe an effective polymerization of the resin. From a practical point of view, the method simply consists in writing several polymer lines into a drop of each resin upon focusing the *fs*-laser beam using a 40x, 0.95-NA objective. By gradually decreasing the laser excitation power, we can then evaluate the minimum deposited energy below which the 2PP is inefficient. **Figure 5** typically shows SEM images of symmetrical patterns of polymer lines written into each

formulation at 800 nm. From the progressive disappearance of the polymer lines as function of the laser excitation power we can estimate that the 2PP energy thresholds (E_{th}) for **ACAR** and **XCAR** formulations are about 42 µJ and 20 µJ, respectively. It is also worth noting that the width of the polymer lines generated for each energy threshold displays an average value in the 240-250 nm range for both formulations as depicted in the insets of **Figure 5**.

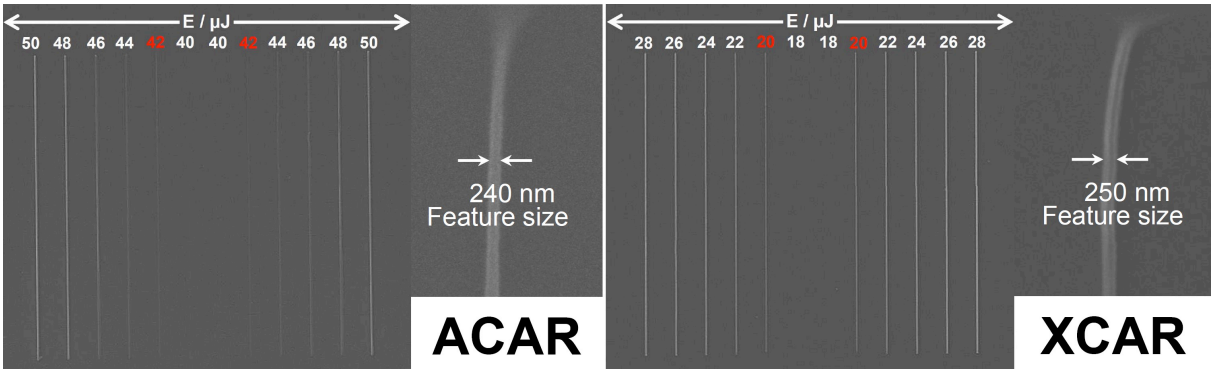

Figure 5. SEM micrographs of 2PP lines fabricated for distinctive laser excitation powers (λ_{ex} = 800 nm). The energy value in red color denotes E_{th} for each formulation. Inset : Magnified SEM images of the polymerized lines generated at E_{th}. Formulation: Isomolar concentration of dye (1.45 mM) and 3 %-w **MDEA**. The resin is an acrylate-based mixing of **PEGDA** (67 mol%) and **PETIA** (33 mol%).

According to the formalism proposed by Baldacchini *et al.*[58], this 2PP threshold energy (E_{th}) can be directly connected to the quantum yield for the generation of primary radicals (Φ_i) owing to the following relationship [3, 58]:

$$[R_0] \propto C.\delta.\Phi_i E_{th}^2 \qquad (2)$$

where C is the concentration of the 2P initiator, [R_0] denotes the local concentration of primary radicals necessary to reach the gelation point. This concentration is expected to be invariant for a given acrylate formulation. Considering the fact that the 2PA cross-sections ratio between **XCAR** and **ACAR** is about ~ 10 at 800 nm, it can be estimated that **ACAR** displays a Φ_i value which is ~ 2.3 times higher than that of **XCAR**. Despite a much weaker 2PA cross-section, **ACAR** exhibits a higher initiation efficiency than **XCAR**. More precisely, the reaction sequence consecutive to the excitation of **ACAR** is likely to generate a much substantial amount of **MDEA•** available for the initiation reaction. In all these reaction sequences, it should be underlined that a significant part of **MDEA•** is consumed by the competing inhibition reaction with oxygen (O_2). Indeed, this latter species which is initially present in the resin is extremely reactive toward the α-aminoalkyl radicals. For instance, the

inhibition rate constant of **MDEA•** by oxygen is typically two orders magnitude higher than that of the free radical addition onto acrylate C=C bonds[59]. In this context, any side reactions allowing the local consumption of dissolved O_2 would indirectly enhance the photoinitiation performance. We are precisely in this case for **ACAR**. This chromophore indeed comprises a 9, 10-disubstitued anthracene subunit, which is prompt to trap oxygen molecule via a well-known [4 + 2] photo cycloaddition[60, 61]. Similarly to the 9,10-diphenyl anthracene[60, 62], the first step of the mechanism (see **Scheme 2**) should imply the photogeneration of a singlet oxygen ($^1O_2$) through a triplet-triplet energy transfer between the excited triplet state of **ACAR** and the oxygen molecule ($^3O_2$).

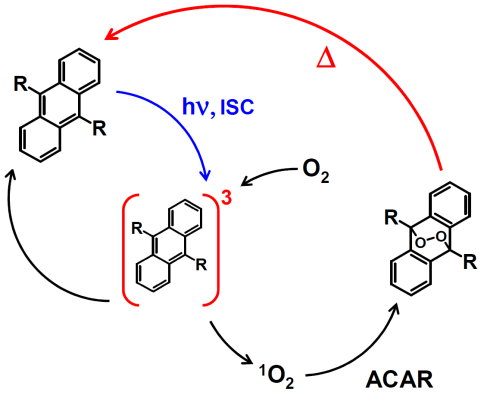

Scheme 2. Global mechanism of the [4+2] photoinduced cycloaddition of $^1O_2$ on ACAR as well as the thermolysis of the generated endoperoxide product.

The quantum yields for singlet oxygen generation (Φ_Δ) have been evaluated for both *o*-carboranes in ethanol using the well known photoxidation method involving the 1,3-diphenylisobenzofuran (**DBF**) used as a very efficient $^1O_2$-sensitive indicator[63]. In this methodology, Rose Bengal (**RB**) was also employed as a reference photosensitizer (Φ_Δ^r = 0.68 in ethanol[63]). Isoabsorbant solutions of *o*-carboranes and **RB** were irradiated at 480 nm in presence of **DBF**. **Figure S5** typically shows the absorbance changes of **DBF** at 425 nm for different short irradiation times. The value of Φ_Δ / Φ_Δ^r can be then derived from the ratio of the corresponding slopes at the initial time of irradiation. According to this photoxidation method, **ACAR** presents a quantum yield for singlet oxygen generation of about 0.05 whereas the corresponding Φ_Δ for **XCAR** is ~ 3-fold lower. Therefore, the excitation of **ACAR** should lead to a more consumption of dissolved O_2 as compared to the corresponding photoreaction with **XCAR**. Interestingly for **ACAR**, the photogenerated singlet oxygen can be chemically trapped according to a second step reaction depicted in **Scheme 2**. This second reaction sequence consists in a cycloaddition of $^1O_2$ into the bridgehead meso positions of **ACAR** with

a consecutive production of an endoperoxide. In order to demonstrate the high sensitivity of **ACAR** to oxygen as compared to **XCAR**, the photolysis of the dyes has been performed in acetonitrile solutions where the concentration of dissolved O_2 was alternatively reduced and increased upon N_2 or air-bubbling. **Figure 6** shows the absorbance time-dependent changes of **ACAR** and **XCAR** at their respective λ_{MAX} during the photolysis reactions at $\lambda_{irr.}$ = 365 nm. First, one clearly observes that the absorption spectrum of **XCAR** remains invariant irrespective to the presence or absence of oxygen. This is a clear indication that **XCAR** does not undergo any photobleaching under our irradiation condition.

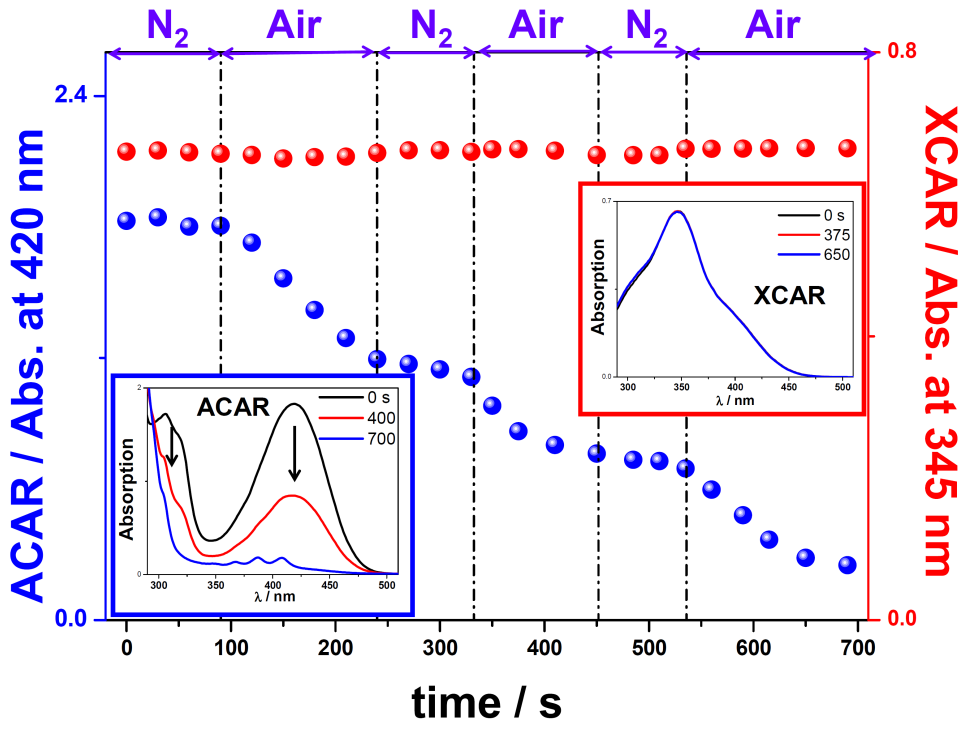

Figure 6. Time-dependent changes of the absorbances of the dyes in acetonitrile solutions in presence or absence of dissolved O_2. Insets: Evolution of the absorption spectrum of the dyes for distinctive irradiation times. ($\lambda_{irr.}$ = 365 nm, P = 120 mW).

By contrast, the continuous irradiation of **ACAR** solution indicates that this chromophore undergoes a photobleaching which is clearly triggered by the presence of oxygen. Whereas the absorption band of the dye remains unchanged within each time interval in N_2-saturated conditions (see **Figure 6**) the introduction of O_2 induces a rapid decrease of its absorption band confirming the consumption of the chromophore. Moreover, the collapse of **ACAR** absorption band gives rise to a new vibronic structured one in the 350-420 nm range which should be assigned to the **ACAR** endoperoxide (see inset **Figure 6**). Interestingly, this anthracene-based 9,10-endoperoxide possesses the capability to regenerate **ACAR** upon

heating [60, 62]. To demonstrate this backward process (see **Scheme 2**), the endoperoxide of **ACAR** was first photogenerated in a DMSO solution similarly to the previous photolysis experiment then heated at 130 °C. As illustrated in **Figure S6A**, the heating of the solution leads to the progressive recovery of the absorption band of **ACAR** as well as its fluorescence. Under our heating conditions, the thermal recovery half-time is about 30 min in DMSO (see **Figure S6B**). As a consequence, **ACAR** constitutes a very interesting two-photon initiator able to meanwhile implement a switchable emissive property into the two-photon patterned materials. As an illustrating example, **Figure 7** shows the fluorescence images from two 2D µ-grids composed of periodic 5 x 5 µm squares two-photon fabricated using **ACAR** and **XCAR** formulations. The **XCAR**-based µ-structure is used as a reference system. The fluorescence emission collected from the µ-grids presumably stems from the remaining dyes embedded into the polymer. As depicted in **Figure 7A**, a complete photobleaching of the dyes is achieved when illuminating the µ-structures during 3 min at 365 nm using a 40x, 0.65-NA objective ($I_{365\ nm}$ = 350 kW cm^{-2}). These two samples were then heated at 130 °C during 5 min. While **XCAR** µ-structure does not display any fluorescence turn-on, a clear recovery of the luminescence signal is nicely observed for the **ACAR**-embedded µ-grid. It should be also noted that further heating of the **XCAR** sample even at higher temperature (e.g. 160 °C) did not lead to any fluorescence return. Note that this irreversible photobleaching indirectly highlights the crucial role of the disubstituted anthracene group within **ACAR** structure. This molecular subunit indeed guarantees the reversible formation of the endoperoxide.

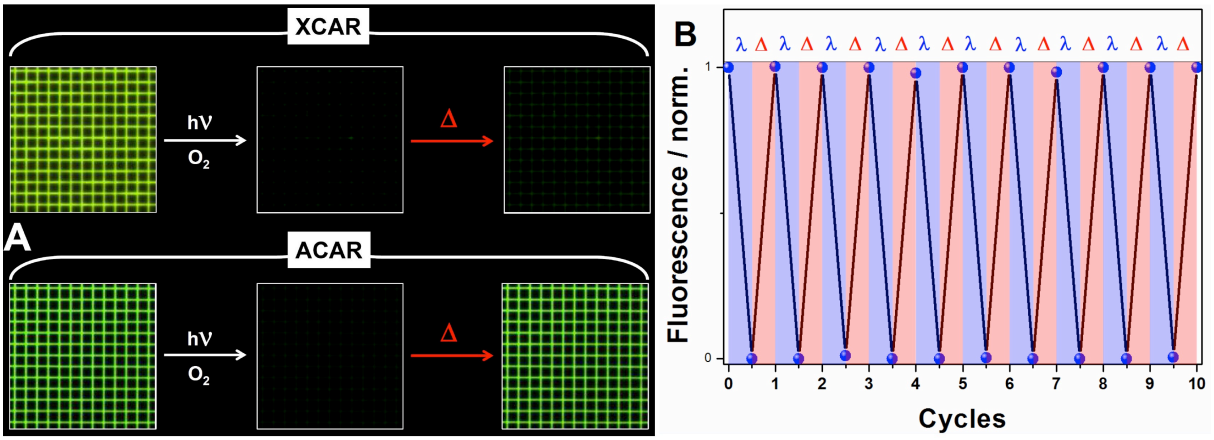

Figure 7. **A.** Comparison of the fluorescence switch processes between **ACAR-** and **XCAR**-based two-photon patterned µ-grids upon a consecutive light-triggered ($\lambda_{irr.}$ = 365 nm during 3 min.) and thermal (130 °C during 5 min) cycle. **B.** Multiple fluorescence turn-off and turn-on cycles for **ACAR** µ-grid upon alternative light- and thermal-induced stimuli ($\lambda_{irr.}$ = 365 nm, 3 min // Δ = 130 °C, 5 min)

Multiple cycles of alternative light- and thermal-stimuli were applied to the **ACAR** µ-grid. As shown in **Figure 7B**, the switchable materials exhibit a very good resistance fatigue after 10 cycles. **Figure S7** shows much more ON/OFF cycles (e.g. 40 cycles) highlighting the robustness and the nice reversibility of the observed commutation. Hence one clearly demonstrates that this original two-photon stereolithography approach allows the 'one pot' direct laser writing of switchable luminescent µ-devices. To illustrate the promising applied potential of our micropatterned strategy in the domain of optical data storage, a 2D matrix composed by an array of 3 x 3 µ-slabs was two-photon patterned using **ACAR** formulation. Each of these nine square slabs with 5 µm side and 1 µm thick can be considered as an independent optical memory unit whose luminescent binary state can be switched via thermal (ON) or light (OFF) stimuli allowing the reversible encoding of the 2D matrix.

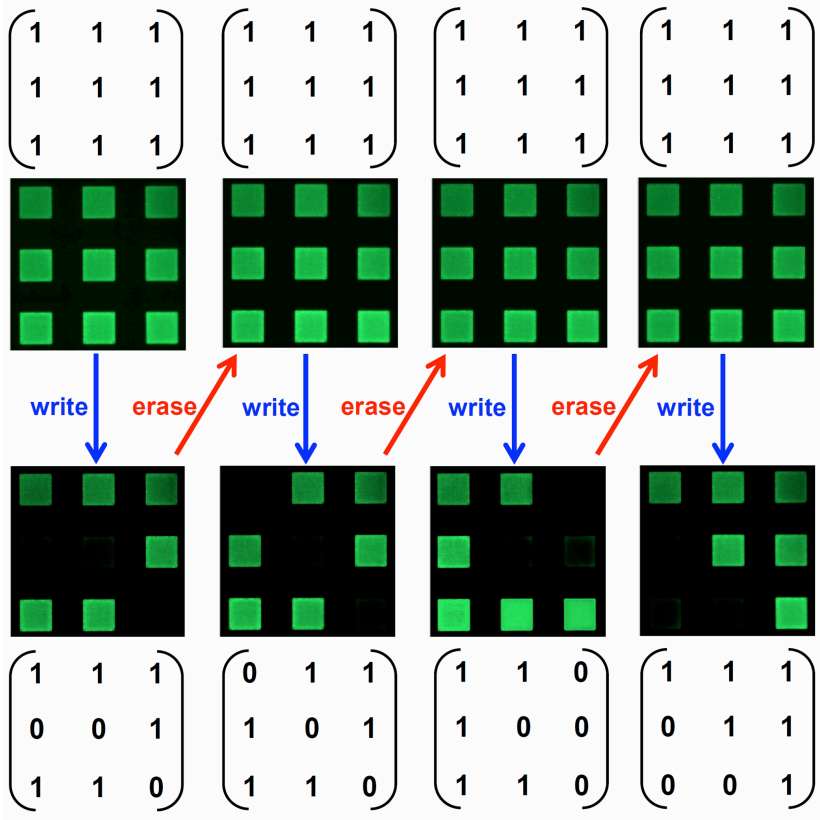

Figure 8. Fluorescence images of a 3 x 3 matrix composed of switchable **ACAR**-embedded µ-slabs (5 µm side) during several distinctive writing-erasing cycles. The writing step corresponds to the irradiation of selected µ-slabs at $\lambda_{irr.}$ = 365 nm during 3 min. The erasing step consists in 5 min heating of the glass coverslip sample at 130 °C.

Such an optical recording sequence is illustrated in **Figure 8**. Starting from a fully luminescent 3 x 3 unit matrix, the writing step consists in encoding an OFF state for three

distinctive components of the matrix by illuminating their corresponding μ-slabs. After the readout of the matrix digital code, all the data can be erased by a simple heating which regenerates the unit matrix for a new writing cycle.

3. CONCLUSION.

The linear and nonlinear photochemical properties of two multibranched *o*-carboranes chromophores have been thoroughly investigated with the objective to account for their two-photon induced reactivity which was oriented toward 3D stereolithography applications. More particularly, the comparison of the dyes 2PP performances lays the stress on an intrinsic superior reactivity of the quadrupolar *o*-carborane derivative as compared to the octupolar homologue, which paradoxically displays a 10 times higher 2PA cross-section. The design of the π-system of **ACAR** bearing carborane acceptor moieties origins a triplet excited state that makes **ACAR** an excellent triplet oxygen scavenger. This unexpected effect stems from an original side reaction specific to the anthracenic quadrupole which can trap the surrounding oxygen via a [4 + 2]-cycloaddition. The subsequent local consumption of the dissolved oxygen in the resin parallely reduces the oxygen inhibition role toward the free radical two-photon polymerization. We demonstrate that this cycloaddition reaction not only improves the 2PP efficiency but also generates an embedded endoperoxide product within the micropatterned polymer. This endoperoxide can regenerate the luminescent *o*-carborane quadrupole upon heating resulting in a fluorescence 'switch-on' of the fabricated µ-structures. Stability of these compounds for materials applications is essential, and the present of boron clusters enhance this robustness. Based on this simple 'one pot' processing approach where all the added value is implemented on the anthracene-based *o*-carborane dye, we have thereby developed an original optical data storage strategy allowing the direct laser writing of switchable materials with robust writing-reading-erasing properties.

4. EXPERIMENTAL SECTION.

4.1 Materials. The synthesis and the characterization of **ACAR** and **XCAR** which have been previously described elsewhere[35, 36] are also detailed in the supporting informations. Polyethylene glycol diacrylate monomer (**PEGDA**, M_n 575) and pentaerythritol triacrylate (**PETIA**), *N*-methyl diethanolamine (**MDEA**), n-tetrabutylammonium hexafluorophosphate (**TBAPF$_6$**), 1,3-diphenylisobenzofuran (**DBF**) and Rose Bengal (**RB**) were purchased from Aldrich. All the solvents which are spectroscopic grade were also purchased from Aldrich.

4.2 Steady-state absorption and fluorescence spectra. The absorption and fluorescence spectra were recorded using a Perkin Elmer Lambda 2 spectrometer and a FluoroMax-4 spectrofluorometer. Emission spectra are spectrally corrected, and fluorescence quantum yields include the correction due to solvent refractive index and were determined relative to quinine bisulfate in 0.05 molar sulfuric acid ($\Phi = 0.52$)[64].

4.3 Fluorescence lifetime measurements. The fluorescence lifetimes were measured using a Nano LED emitting at 372 nm as an excitation source with a nano led controller module, Fluorohub from IBH, operating at 1MHz. The detection was based on an R928P type photomultiplier from Hamamatsu with high sensitivity photon-counting mode. The decays were fitted with the iterative reconvolution method on the basis of the Marquardt/Levenberg algorithm[65]. Such a reconvolution technique allows an overall-time resolution down to 0.2 ns. The quality of the exponential fits was checked using the reduced χ^2 (≤ 1.2)

4.4 Low-temperature measurements. Low-temperature emission measurements were performed in 2MTHF using a Oxford Cryogenics OptistatDN cryostat fitted with a Oxford Instruments ITC503S temperature controller. The temperature dependency of the refractive index and the density of the solvent were taken into account for the measurement of Φ_f [66].

4.5 ESR spin trapping (ESR-ST) experiment. Electron spinning resonance spin trapping (ESR-ST) experiments carried out by a Bruker EMX-plus spectrometer (X-band). The radicals generated when exposed to LED light source (365nm) at room temperature under Argon and were trapped by phenyl N-tert-butylnitrone (PBN) in *tert*-butyl benzene.

4.6 Two-photon excitation fluorescence. The two-photon absorption (2PA) measurements were performed with femtosecond mode-locked laser pulse using a Ti: Sapphire laser (Coherent, Chameleon Ultra II: pulse duration: ~140 fs; repetition rate: 80 MHz; wavelength range: 680-1040 nm). A relative two-photon excited fluorescence method[67] was employed to measure the two-photon absorption cross-sections, δ. The measurements of 2PA cross-sections were performed relative to reference molecules (*r*) such as fluorescein[68-70] in water at pH = 11. The value of δ for a sample (*s*) is given by:

$$\delta_S = \frac{S_S \Phi_r \eta_r c_r}{S_r \Phi_S \eta_S c_S} . \delta_r$$

Where *S* is the detected two-photon excited fluorescence integral area, *c* the concentration of the chromophores, and Φ is the fluorescence quantum yield of the chromophores. η is the collection efficiency of the experimental set-up and accounts for the wavelength dependence of the detectors and optics as well as the difference in refractive indices between the solvents in which the reference and sample compounds are dissolved. The measurements were conducted in a regime where the fluorescence signal showed a quadratic dependence on the intensity of the excitation beam, as expected for two-photon induced emission. For the calibration of the two-photon absorption spectra, the two-photon excited fluorescence signal of each compound was recorded at the same excitation wavelength as that used for standards (i.e. λ_{exc} = 782 nm for fluorescein). The laser intensity was in the range of 0.2-2 x 10^9 W/cm^2. The experimental error on the reported cross section is 15 %.

4.7 Two-Photon lithography. The 3D lithographic microfabrication was carried out using a Zeiss Axio Observer D1 inverted microscope. The two-photon excitation was performed at 800 nm using respectively a mode-locked Ti: Sapphire oscillator (Coherent, Chameleon Ultra II: pulse duration: ~140 fs; repetition rate: 80 MHz). The incident beam was focused through a 0.95 NA objective (40 X) which leads to a radial spot size 450 nm at λ_{exc} = 800 nm (1/e^2 Gaussian). A drop of the resin is deposited on a cover slip which is mounted on a 3D piezoelectric stage allowing the translation relative to the laser focal point. The intensity of the entering laser is controlled with the use of an acousto optic modulator. The displacement of the sample and all photonic parameters (i.e. excitation power and irradiation times) are computer-controlled. The 3D microstructure is finally obtained by washing away the unexposed monomer resin using ethanol.

4.8 Fluorescence image microscopy. The multiple cycles relative to the fluorescence turn-on / turn-off from the two-photon patterned µ-structures were monitored using fluorescence microscopy. The glass coverslip with the µ-structures was positioned on an Olympus IX73 inverted microscope equipped with a 75 W Xe lamp housing. The sample was then excited from the bottom of the sample at $\lambda_{exc.}$ = 365 nm through a 40X, 0.65-NA objective using an Olympus U-FUN fluorescence mirror unit composed of a 365 nm band pass filter (BP360-370), a dichroic mirror (DM410) and long pass filter (BA420IF). The epifluorescence signal from the photopatterned sample is collected by the same objective, passes through the same fluorescence mirror unit and collected by a CMOS camera (ORCA-

Flash4.0 from Hamamatsu). For each light-triggered fluorescence turn-off step, the time-dependent emission decrease from the excited sample was recorded through a series of time-lapse epifluorescence images. For each fluorescence turn-on step, the sample was first heated during 5 min at 130 °C on a heating plate then similarly repositioned on inverted microscope for the next turn-off step.

4.9 Cyclic voltammetry. The redox potentials of the compounds were measured by cyclic voltammetry using a Radiometer Voltalab 6 potentiostat. All measurements were performed at 300 K in N_2-saturated dichloromethane (**DCM**) with 0.1 M of **$TBAPF_6$** used as supporting electrolyte. The cyclic voltammograms (CVs) were recorded using a three-electrode cell with a platinum disk as working electrode. A platinum wire was used as auxiliary electrode. A saturated calomel electrode (SCE) used as a reference was placed in a separate compartment with a salt bridge containing the supporting electrolyte. Ferrocene (Fc) was used as an internal reference (considering $E_{Fc/Fc+}$ = + 0.53 V in **DCM** *vs.* aqueous SCE[71]).

NOTES.

The authors declare no competing financial interest.

ASSOCIATED CONTENT

Supporting Information. Fluorescence spectra of **ACAR** and **XCAR** in high and low temperature regions of 2MTHF. Cyclic voltamogramms of *o*-carboranes and **MDEA** in dichloromethane. Screening test structure to evaluate the maximum two-photon writing speeds of **ACAR** and **XCAR** formulations. Determination of quantum yields singlet oxygen generation of o-carborane derivatives in ethanol. Fluorescence and absorption spectra recovery of **ACAR** by heating a solution of its endoperoxide in DMSO at 130°C. Multiple ON/OFF fluorescence switches from an **ACAR** embedded μ-grid during alternative light- and thermal-induced stimuli. Synthesis and characterisation of **ACAR** and **XCAR**.

ACKNOWLEDGMENTS

This work was financially supported by MICINN (PID2019-106832RB-I00 and the Severo Ochoa Program for Centers of Excellence for the FUNFUTURE CEX2019-000917-S project) and by Generalitat de Catalunya (2021-SGR00442)

REFERENCE.

1. Lay, C. L.; Koh, C. S. L.; Lee, Y. H.; Phan-Quang, G. C.; Sim, H. Y. F.; Leong, S. X.; Han, X.; Phang, I. Y.; Ling, X. Y., Two-Photon-Assisted Polymerization and Reduction: Emerging Formulations and Applications. *ACS Appl. Mater. Interfaces* **2020,** 12, (9), 10061-10079.

2. Barner-Kowollik, C.; Bastmeyer, M.; Blasco, E.; Delaittre, G.; Müller, P.; Richter, B.; Wegener, M., 3D Laser Micro- and Nanoprinting: Challenges for Chemistry. *Angew. Chem. Int. Ed.* **2017,** 56, (50), 15828-15845.

3. LaFratta, C. N.; Fourkas, J. T.; Baldacchini, T.; Farrer, R. A., Multiphoton Fabrication. *Angew. Chem. Int. Ed.* **2007,** 46, (33), 6238-6258.

4. Ding, H.; Zhang, Q.; Gu, H.; Liu, X.; Sun, L.; Gu, M.; Gu, Z., Controlled Microstructural Architectures Based on Smart Fabrication Strategies. *Adv. Funct. Mater.* **2020,** 30, (2), 1901760.

5. O'Halloran, S.; Pandit, A.; Heise, A.; Kellett, A., Two-Photon Polymerization: Fundamentals, Materials, and Chemical Modification Strategies. *Adv. Sci.* **2022,** 10, (7), 2204072.

6. Schaedler, T. A.; Jacobsen, A. J.; Torrents, A.; Sorensen, A. E.; Lian, J.; Greer, J. R.; Valdevit, L.; Carter, W. B., Ultralight Metallic Microlattices. *Science* 334, (6058), 962-965.

7. Mei, J.; Ma, G.; Yang, M.; Yang, Z.; Wen, W.; Sheng, P., Dark acoustic metamaterials as super absorbers for low-frequency sound. *Nat. Commun.* **2012,** 3, (1), 756.

8. Linden, S.; Enkrich, C.; Wegener, M.; Zhou, J.; Koschny, T.; Soukoulis, C. M., Magnetic Response of Metamaterials at 100 Terahertz. *Science* **2004,** 306, (5700), 1351-1353.

9. Kenanakis, G.; Xomalis, A.; Selimis, A.; Vamvakaki, M.; Farsari, M.; Kafesaki, M.; Soukoulis, C. M.; Economou, E. N., Three-Dimensional Infrared Metamaterial with Asymmetric Transmission. *ACS Photonics* **2015,** 2, (2), 287-294.

10. Silva, A.; Monticone, F.; Castaldi, G.; Galdi, V.; Alu, A.; Engheta, N., Performing Mathematical Operations with Metamaterials. *Science* **2014,** 343, (6167), 160-163.

11. Torgersen, J.; Qin, X.-H.; Li, Z.; Ovsianikov, A.; Liska, R.; Stampfl, J., Hydrogels for Two-Photon Polymerization: A Toolbox for Mimicking the Extracellular Matrix. *Adv. Funct. Mater.* **2013,** 23, (36), 4542-4554.

12. Xing, J.-F.; Zheng, M.-L.; Duan, X.-M., Two-photon polymerization microfabrication of hydrogels: an advanced 3D printing technology for tissue engineering and drug delivery. *Chem. Soc. Rev.* **2015,** 44, (15), 5031-5039.

13. Huang, T.-Y.; Sakar, M. S.; Mao, A.; Petruska, A. J.; Qiu, F.; Chen, X.-B.; Kennedy, S.; Mooney, D.; Nelson, B. J., 3D Printed Microtransporters: Compound Micromachines for Spatiotemporally Controlled Delivery of Therapeutic Agents. *Adv. Mater.* **2015,** 27, (42), 6644-6650.

14. Hippler, M.; Blasco, E.; Qu, J.; Tanaka, M.; Barner-Kowollik, C.; Wegener, M.; Bastmeyer, M., Controlling the shape of 3D microstructures by temperature and light. *Nat. Commun.* **2019,** 10, (1), 232.

15. Lv, C.; Sun, X.-C.; Xia, H.; Yu, Y.-H.; Wang, G.; Cao, X.-W.; Li, S.-X.; Wang, Y.-S.; Chen, Q.-D.; Yu, Y.-D.; Sun, H.-B., Humidity-responsive actuation of programmable hydrogel microstructures based on 3D printing. *Sens Actuators B Chem.* **2018,** 259, 736-744.

16. Sun, X.-C.; Xia, H.; Xu, X.-L.; Lv, C.; Zhao, Y., Ingenious humidity-powered micro-worm with asymmetric biped from single hydrogel. *Sens Actuators B Chem.* **2020,** 322, 128620.

17. Blasco, E.; Müller, J.; Müller, P.; Trouillet, V.; Schön, M.; Scherer, T.; Barner-Kowollik, C.; Wegener, M., Fabrication of Conductive 3D Gold-Containing Microstructures via Direct Laser Writing. *Adv. Mater.* **2016,** 28, (18), 3592-3595.

18. Tabrizi, S.; Cao, Y.; Cumming, B. P.; Jia, B.; Gu, M., Functional Optical Plasmonic Resonators Fabricated via Highly Photosensitive Direct Laser Reduction. *Adv. Opt. Mater.* **2016,** 4, (4), 529-533.

19. Lee, M. R.; Lee, H. K.; Yang, Y.; Koh, C. S. L.; Lay, C. L.; Lee, Y. H.; Phang, I. Y.; Ling, X. Y., Direct Metal Writing and Precise Positioning of Gold Nanoparticles within Microfluidic Channels for SERS Sensing of Gaseous Analytes. *ACS Appl. Mater. Interfaces* **2017,** 9, (45), 39584-39593.

20. Xu, B.-B.; Zhang, R.; Liu, X.-Q.; Wang, H.; Zhang, Y.-L.; Jiang, H.-B.; Wang, L.; Ma, Z.-C.; Ku, J.-F.; Xiao, F.-S.; Sun, H.-B., On-chip fabrication of silver microflower arrays as a catalytic microreactor for allowing in situ SERS monitoring. *Chem. Commun.* **2012,** 48, (11), 1680-1682.

21. Versace, D.-L.; Moran, G.; Belqat, M.; Spangenberg, A.; Meallet-Renault, R.; Abbad-Andaloussi, S.; Brezova, V.; Malval, J.-P., Highly Virulent Bactericidal Effects of Curcumin-based μ-Cages Fabricated by Two-Photon Polymerization. *ACS Appl. Mater. Interfaces* **2020,** 12, 5050-5057.

22. Mhanna, R.; Durand, N.; Savel, P.; Akdas-Kiliç, H.; Abdallah, S.; Versace, D.-L.; Soppera, O.; Fillaut, J.-L.; Sojic, N.; Malval, J.-P., Micropatterning of electrochemiluminescent polymers based on multipolar Ru-complex two-photon initiators. *Chem. Commun.* **2022,** 58, (69), 9678-9681.

23. Núñez, R.; Tarrés, M. r.; Ferrer-Ugalde, A.; de Biani, F. F.; Teixidor, F., Electrochemistry and Photoluminescence of Icosahedral Carboranes, Boranes, Metallacarboranes, and Their Derivatives. *Chem. Rev.* **2016,** 116, (23), 14307-14378.

24. Cabrera-González, J.; Ferrer-Ugalde, A.; Bhattacharyya, S.; Chaari, M.; Teixidor, F.; Gierschner, J.; Núñez, R., Fluorescent carborane-vinylstilbene functionalised octasilsesquioxanes: synthesis, structural, thermal and photophysical properties. *J. Mater. Chem. C* **2017,** 5, (39), 10211-10219.

25. Cabrera-González, J.; Cabana, L.; Ballesteros, B.; Tobias, G.; Núñez, R., Highly Dispersible and Stable Anionic Boron Cluster-Graphene Oxide Nanohybrids. *Chem. Eur. J.* **2016,** 22, (15), 5096-5101.

26. Cabrera-González, J.; Sánchez-Arderiu, V.; Viñas, C.; Parella, T.; Teixidor, F.; Núñez, R., Redox-Active Metallacarborane-Decorated Octasilsesquioxanes. Electrochemical and Thermal Properties. *Inorg. Chem.* **2016,** 55, (22), 11630-11634.

27. Núñez, R.; Romero, I.; Teixidor, F.; Viñas , C., Icosahedral boron clusters: a perfect tool for the enhancement of polymer features. *Chem. Soc. Rev.* **2016,** 45, (19), 5147-5173.

28. Fernandez-Alvarez, R.; Hlavatovičová, E.; Rodzeń , K.; Strachota, A.; Kereïche, S.; Matějíček, P.; Cabrera-González, J.; Núñez , R.; Uchman, M., Synthesis and self-assembly of a carborane-containing ABC triblock terpolymer: morphology control on a dual-stimuli responsive system. *Polym. Chem.* **2019,** 10, (22), 2774-2780.

29. Naito, H.; Morisaki, Y.; Chujo, Y., o-Carborane-Based Anthracene: A Variety of Emission Behaviors. *Angew. Chem. Int. Ed.* **2015,** 54, (17), 5084-5087.

30. Mukherjee, S.; Thilagar, P., Boron clusters in luminescent materials. *Chem. Commu.* **2016,** 52, (6), 1070-1093.

31. Ferrer-Ugalde, A.; Gonzalez-Campo, A.; Vinas, C.; Rodriguez-Romero, J.; Santillan, R.; Farfan, N.; Sillanpaa, R.; Sousa-Pedrares, A.; Núñez, R.; Teixidor, F., Fluorescence of New o-Carborane Compounds with Different Fluorophores: Can it be Tuned? *Chem. Eur. J.* **2014,** 20, (32), 9940-9951.

32. Peterson, J. J.; Davis, A. R.; Werre, M.; Coughlin, E. B.; Carter, K. R., Carborane-Containing Poly(fluorene): Response to Solvent Vapors and Amines. *ACS Appl. Mater. Interfaces* **2011,** 3, (6), 1796-1799.

33. Terenziani, F.; Katan, C.; Badaeva, E.; Tretiak, S.; Blanchard-Desce, M., Enhanced Two-Photon Absorption of Organic Chromophores: Theoretical and Experimental Assessments. *Adv. Mater.* **2008,** 20, (24), 4641-4678.

34. Katan, C.; Terenziani, F.; Mongin, O.; Werts, M. H. V.; Porrès, L.; Pons, T.; Mertz, J.; Tretiak, S.; Blanchard-Desce, M., Effects of (Multi)branching of Dipolar Chromophores on Photophysical Properties and Two-Photon Absorption. *J. Phys. Chem. A* **2005,** 109, (13), 3024-3037.

35. Chaari, M.; Cabrera-González, J.; Kelemen, Z.; Vinas, C.; Ferrer-Ugalde, A.; Choquesillo-Lazarte, D.; Ben Salah, A.; Teixidor, F.; Núñez, R., Luminescence properties of carborane-containing distyrylaromatic systems. *J. Organomet. Chem.* **2018,** 865, 206-213.

36. Cabrera-González, J.; Bhattacharyya, S.; Milian-Medina, B.; Teixidor, F.; Farfan, N.; Arcos-Ramos, R.; Vargas-Reyes, V.; Gierschner, J.; Núñez, R., Tetrakis{[(p-dodecacarboranyl)methyl]stilbenyl}ethylene: A Luminescent Tetraphenylethylene (TPE) Core System. *Eur. J. Inorg. Chem.* **2017,** 2017, (38-39), 4575-4580.

37. Savel, P.; Akdas-Kilig, H.; Malval, J.-P.; Spangenberg, A.; Roisnel, T.; Fillaut, J.-L., Metal-induced dimensionality tuning in a series of bipyrimidine-based ligands: a tool to enhance two-photon absorption. *J. Mater. Chem. C* **2014,** 2, (2), 295-305.

38. Akdas-Kilig, H.; Godfroy, M.; Fillaut, J.-L.; Donnio, B.; Heinrich, B.; Kedziora, P.; Malval, J.-P.; Spangenberg, A.; Van Cleuvenbergen, S.; Clays, K.; Camerel, F., Mesogenic, Luminescence, and Nonlinear Optical Properties of New Bipyrimidine-Based Multifunctional Octupoles. *J. Phys. Chem. C* **2015,** 119, (7), 3697-3710.

39. Zhang, X.-B.; Feng, J.-K.; Ren, A.-M., Theoretical Study of One- and Two-Photon Absorption Properties of Octupolar D2d and D3 Bipyridyl Metal Complexes. *J. Phys. Chem. A* **2007,** 111, (7), 1328-1338.

40. Lambert, C.; Schmälzlin, E.; Meerholz, K.; Bräuchle, C., Synthesis and Nonlinear Optical Properties of Three-Dimensional Phosphonium Ion Chromophores. *Chem. Eur. J.* **1998,** 4, (3), 512-521.

41. Katan, C.; Tretiak, S.; Werts, M. H. V.; Bain, A. J.; Marsh, R. J.; Leonczek, N.; Nicolaou, N.; Badaeva, E.; Mongin, O.; Blanchard-Desce, M., Two-Photon Transitions in Quadrupolar and Branched Chromophores: Experiment and Theory. *J. Phys. Chem. B* **2007,** 111, (32), 9468-9483.

42. Grabowski, Z. R.; Rotkiewicz, K.; Rettig, W., Structural Changes Accompanying Intramolecular Electron Transfer: Focus on Twisted Intramolecular Charge-Transfer States and Structures. *Chem. Rev.* **2003,** 103, (10), 3899-4032.

43. Furutsuka, T.; Imura, T.; Kojima, T.; Kawabe, K., Dielectric Constant of 2-Methyltetrahydrofuran. *Techn. Rep. Osaka Univ.* **1974**, 367.

44. Goes, M.; de Groot, M.; Koeberg, M.; Verhoeven, J. W.; Lokan, N. R.; Shephard, M. J.; Paddon-Row, M. N., Temperature Dependence of Charge-Transfer Fluorescence from Extended and U-shaped Donor-Bridge-Acceptor Systems in Glass-Forming Solvents *J. Phys. Chem. A* **2001,** 106, (10), 2129-2134.

45. Bublitz, G. U.; Boxer, S. G., Effective Polarity of Frozen Solvent Glasses in the Vicinity of Dipolar Solutes. *J. Am. Chem. Soc.* **1998,** 120, (16), 3988-3992.

46. Letard, J. F.; Lapouyade, R.; Rettig, W., Structure-photophysics correlations in a series of 4-(dialkylamino)stilbenes: intramolecular charge transfer in the excited state as related to the twist around the single bonds. *J. Am. Chem. Soc.* **1993,** 115, (6), 2441-2447.

47. Lapouyade, R.; Czeschka, K.; Majenz, W.; Rettig, W.; Gilabert, E.; Rulliere, C., Photophysics of donor-acceptor substituted stilbenes. A time-resolved fluorescence study using selectively bridged dimethylamino cyano model compounds. *J. Phys. Chem.* **1992,** 96, (24), 9643-9650.

48. El-Gezawy, H.; Rettig, W.; Lapouyade, R., Solvatochromic Behavior of Donor-Acceptor-Polyenes: Dimethylamino-cyano-diphenylbutadiene. *J. Phys. Chem. A* **2005,** 110, (1), 67-75.

49. Cheng, C.-C.; Yu, W.-S.; Chou, P.-T.; Peng, S.-M.; Lee, G.-H.; Wu, P.-C.; Song, Y.-H.; Chi, Y., Syntheses and remarkable photophysical properties of 5-(2-pyridyl) pyrazolate boron complexes; photoinduced electron transfer. *Chem. Commun.* **2003,** 0, (20), 2628-2629.

50. Fouassier, J. P.; Lalevée, J., *Photoinitiator for Polymer Synthesis-Scope, Reactivity and Efficiency*. Wiley-VCH Berlag GmbH & Co.: Weinheim, 2012.

51. Miao, W.; Choi, J.-P.; Bard, A. J., Electrogenerated Chemiluminescence 69:The Tris(2,2'-bipyridine)ruthenium(II), (Ru(bpy)32+)/Tri-n-propylamine (TPrA) System Revisited A New Route Involving TPrA+ Cation Radicals. *J. Am. Chem. Soc.* **2002,** 124, (48), 14478-14485.

52. Fischer, H.; L.Radom, Factors Controlling The Addition of Cabon-Centered Radicals to Alkenes-An Experimental and Theoretical Perspective. *Angew. Chem. Int. Ed.* **2001,** 40, 1340-1371.

53. Kotake, Y.; Kuwata, K., Electron Spin Resonance Study on the Difference of Structure in Diastereomeric Nitroxyl Radicals. *Bull. Chem. Soc. Jpn.* **1981,** 54, 394-398.

54. Lunzer, M.; Beckwith, J. S.; Chalupa-Gantner, F.; Rosspeintner, A.; Licari, G.; Steiger, W.; Hametner, C.; Liska, R.; Fröhlich, J.; Vauthey, E.; Ovsianikov, A.; Holzer, B., Beyond the Threshold: A Study of Chalcogenophene-Based Two-Photon Initiators. *Chem. Mater.* **2022,** 34, (7), 3042-3052.

55. Li, Z.; Pucher, N.; Cicha, K.; Torgersen, J.; Ligon, S. C.; Ajami, A.; Husinsky, W.; Rosspeintner, A.; Vauthey, E.; Naumov, S.; Scherzer, T.; Stampfl, J.; Liska, R., A Straightforward Synthesis and Structure-Activity Relationship of Highly Efficient Initiators for Two-Photon Polymerization. *Macromolecules* **2013,** 46, (2), 352-361.

56. Li, Z.; Siklos, M.; Pucher, N.; Cicha, K.; Ajami, A.; Husinsky, W.; Rosspeintner, A.; Vauthey, E.; Gescheidt, G.; Stampfl, J.; Liska, R., Synthesis and structure-activity relationship of several aromatic ketone-based two-photon initiators. *J. Polym. Sci. A Polym. Chem.* **2011,** 49, (17), 3688-3699.

57. Pucher, N.; Rosspeintner, A.; Satzinger, V.; Schmidt, V.; Gescheidt, G.; Stampfl, J.; Liska, R., Structure-Activity Relationship in D-π-A-π-D-Based Photoinitiators for the Two-Photon-Induced Photopolymerization Process. *Macromolecules* **2009,** 42, (17), 6519-6528.

58. Baldacchini, T.; LaFratta, C. N.; Farrer, R. A.; Teich, M. C.; Saleh, B. E. A.; Naughton, M. J.; Fourkas, J. T., Acrylic-based resin with favorable properties for three-dimensional two-photon polymerization. *J. Appl. Phys.* **2004,** 95, (11), 6072-6076.

59. Ligon, S. C.; Husar, B.; Wutzel, H.; Holman, R.; Liska, R., Strategies to Reduce Oxygen Inhibition in Photoinduced Polymerization. *Chem. Rev.* **2014,** 114, (1), 557-589.

60. Aubry, J.-M.; Pierlot, C.; Rigaudy, J.; Schmidt, R., Reversible Binding of Oxygen to Aromatic Compounds. *Acc. Chem. Res.* **2003,** 36, (9), 668-675.

61. Clennan, E. L., Synthetic and mechanistic aspects of 1,3-diene photooxidation. *Tetrahedron* **1991,** 47, (8), 1343-1382.

62. Fudickar, W.; Fery, A.; Linker, T., Reversible Light and Air-Driven Lithography by Singlet Oxygen. *J. Am. Chem. Soc.* **2005,** 127, (26), 9386-9387.

63. DeRosa, M. C.; Crutchley, R. J., Photosensitized singlet oxygen and its applications. *Coord. Chem. Rev.* **2002,** 233-234, 351-371.

64. Meech, R.; Phillips, D., Photophysics of some common fluorescence standards. *J. Photochem.* **1983,** 23, 193–217.

65. Connor, D. V.; Phillips, D., *Time correlated single photon counting* , Academic Press: London, 1984.

66. Rong-Ri, T.; Xin, S.; Lin, H.; Feng-Shou, Z., Liquid-to-glass transition of tetrahydrofuran and 2-methyltetrahydrofuran. *Chin. Phys. B* **2012,** 21, 086402.

67. Xu, C.; Webb, W. W., Measurement of two-photon excitation cross sections of molecular fluorophores with data from 690 to 1050 nm. *J. Opt. Soc. Am. B* **1996,** 13, 481-491.

68. Albota, M. A.; Xu, C.; Webb, W. W., Two-Photon Fluorescence Excitation Cross Sections of Biomolecular Probes from 690 to 960 nm. *Appl. Opt.* **1998,** 37, (31), 7352-7356.

69. Makarov, N. S.; Drobizhev, M.; Rebane, A., Two-photon absorption standards in the 550-1600 nm excitation wavelength range. *Opt. Express* **2008,** 16, (6), 4029-4047.

70. De Reguardati, S.; Pahapill, J.; Mikhailov, A.; Stepanenko, Y.; Rebane, A., High-accuracy reference standards for two-photon absorption in the 680-1050 nm wavelength range. *Opt. Express* **2016,** 24, (8), 9053-9066.

71. Hapiot, P.; Kispert, L. D.; Konovalov, V. V.; Savéant, J.-M., Single Two-Electron Transfers vs Successive One-Electron Transfers in Polyconjugated Systems Illustrated by the Electrochemical Oxidation and Reduction of Carotenoids. *J. Am. Chem. Soc.* **2001,** 123, (27), 6669-6677.

TABLE OF CONTENTS ENTRY.